Research Article

Seong-Hwang Kim, Sun-Min Park*, and Soo-Jin Park*

Role of dry ozonization of basalt fibers on interfacial properties and fracture toughness of epoxy matrix composites

https://doi.org/10.1515/ntrev-2021-0048
received March 31, 2021; accepted June 7, 2021

Abstract: The mechanical properties of basalt fiber-reinforced epoxy composites (BFRPs) are significantly dependent on the interfacial adhesion between basalt fibers (BFs) and the epoxy matrix. In this study, we proposed a simple and efficient method for deep and stable penetration of BFs into the epoxy matrix through dry-ozone treatments. To confirm the efficiency of the proposed method, BFRPs were fabricated using two types of composites: untreated BFs and dry-ozonized BFs in varying amounts, and the optimum amount of BFs for all the composites fabricated in this work was 60 wt%. With the addition of this amount of dry-ozonized BFs, the interlaminar shear strength and fracture toughness of the composites were enhanced by 21.2 and 23.2%, respectively, as compared with untreated BFs. The related reinforcing mechanisms were also analyzed, and the enhanced interfacial adhesion was mainly attributed to the mechanical interlocking effect. This approach shows that the dry-ozone treatment of BFs is a simple and efficient method for the preparation of BFRPs with excellent interfacial adhesion, which can be a potential application in the auto parts industry.

Keywords: basalt fiber-reinforced polymer composites, interfacial properties, fracture toughness

*** Corresponding author: Sun-Min Park,** Department of Fibrous Ceramics & Aerospace Material, Korea Institute of Ceramic Engineering and Technology, Jinju 52851, Republic of Korea, e-mail: psm@kicet.re.kr, tel: +82-55-792-2624, fax: +82-55-792-2530
*** Corresponding author: Soo-Jin Park,** Department of Chemistry, Inha University, 100 Inharo, Incheon 22212, Republic of Korea, e-mail: sjpark@inha.ac.kr, tel: +82-32-876-7234, fax: +82-32-860-8438
Seong-Hwang Kim: Department of Chemistry, Inha University, 100 Inharo, Incheon 22212, Republic of Korea

1 Introduction

Currently, carbon fiber-reinforced polymer composites (CFRPs) are being extensively studied owing to their superior mechanical properties [1–6]. However, while CFRPs can reduce vehicle weight by 30–60%, the cost of the overall process is not currently economically viable [7,8]. Recently, basalt fibers (BFs) have attracted considerable attention as reinforcement in polymer-based composites and auto parts industry because it is eco-friendly, nontoxic, easy to process, and costs less than carbon fibers (CFs) [9–12].

However, poor interfacial interaction of the fiber surfaces, particularly for BFs with chemically inert surfaces, makes incorporation within a polymer matrix difficult due to low wettability, resulting in poor interfacial adhesion [13,14]. Several recent studies have confirmed that surface modification was utilized to overcome these challenges in basalt fiber-reinforced polymer composites (BFRPs) [15–17]. In this regard, Lee *et al.* [18] demonstrated that acid treatment can promote the chemical reaction of BFs with an epoxy matrix. In addition, Kim *et al.* [19] demonstrated that plasma-treated BFs enhance the interlaminar shear strength (ILSS) of BFRPs. As is well known, high concentration acid and plasma treatment has shown promising results to improve interfacial adhesions onto BFRPs. However, it has been reported that defects/damage are unavoidably introduced onto the fiber surfaces when exposing fibers to plasma irradiation [20]. In addition, the high concentration acid requires strong acids or harmful chemicals, and consequently, fibers contain traces of undesirable chemicals and thus require further purification [21]. While both of these methods have demonstrated to be efficacious, they still have some drawbacks when applied to practical applications.

Dry-ozone treatment is an eco-friendly and straightforward process as compared with the other surface functionalization techniques [22,23]. This treatment method can be performed in an atmospheric condition and can enhance the interfacial adhesions by inducing oxygen-

containing functional groups through the O_3 oxidation process [24,25]. In this respect, Downey and Drzal [26] modified CF surfaces using ozone treatment and found the enhanced interface and mechanical properties of CFRPs. Considering the above facts, not only do various functional groups on the dry-ozonized BFs enhance wettability with the epoxy matrix, but they can also act as reactive sites for further promotion of interfacial adhesion between the BFs and the epoxy matrix.

The aim of the present research is to explore the potential of BFRPs fabricated from dry-ozonized BFs, which provides new types of economical and eco-friendly composites. Herein, the chemical and morphological changes of dry-ozonized BFs were investigated, and the effects of dry-ozonized BFs on the interfacial adhesion and fracture toughness of the composites are evaluated. Such an effort could result in the conversion of auto parts into fiber-reinforced polymer composites (FRPs) and provide a rational solution toward determining the theoretical limits of composite interfaces.

2 Experimental

2.1 Materials

Unless otherwise stated, chemicals were obtained from a commercial company and were used without further purification. BFs (chopped-type, a diameter of 0.5 mm and length of 4.0 mm, F260 grade) were purchased from Secotech Co., Korea. Epoxy resin (density: ~1.16 g cm^{-3} at 25°C and epoxide equivalent weight: 185–190 g eq^{-1}) was purchased from Kukdo Co., Korea. A 4,4′-diaminodiphenylmethane (DDM) curing agent was purchased from Tokyo Chemical Co., Japan.

2.2 Dry-ozone treatment of BFs

Figure 1(a) illustrates the dry-ozone treatment process. An Ozonetech Lab-Series ozone generator was used for the production of ozone from dry and pure O_2 as the gas source. The oxygen flow rate to the generator was maintained at 0.8 L min^{-1} and monitored with a rotameter incorporated into the ozone generator. The diffusion rate of the O_3 gas, introduced from the bottom of the ozone chamber through a sintered metal diffusing plate, was 8 g h^{-1} and was measured at room temperature for 4 h [20]. The dry-ozonized BFs were denoted as OBFs.

2.3 Fabrication of OBFs/epoxy composites

Figure 1(b) illustrates the OBF/epoxy composite preparation process. First, different concentrations of BFs or

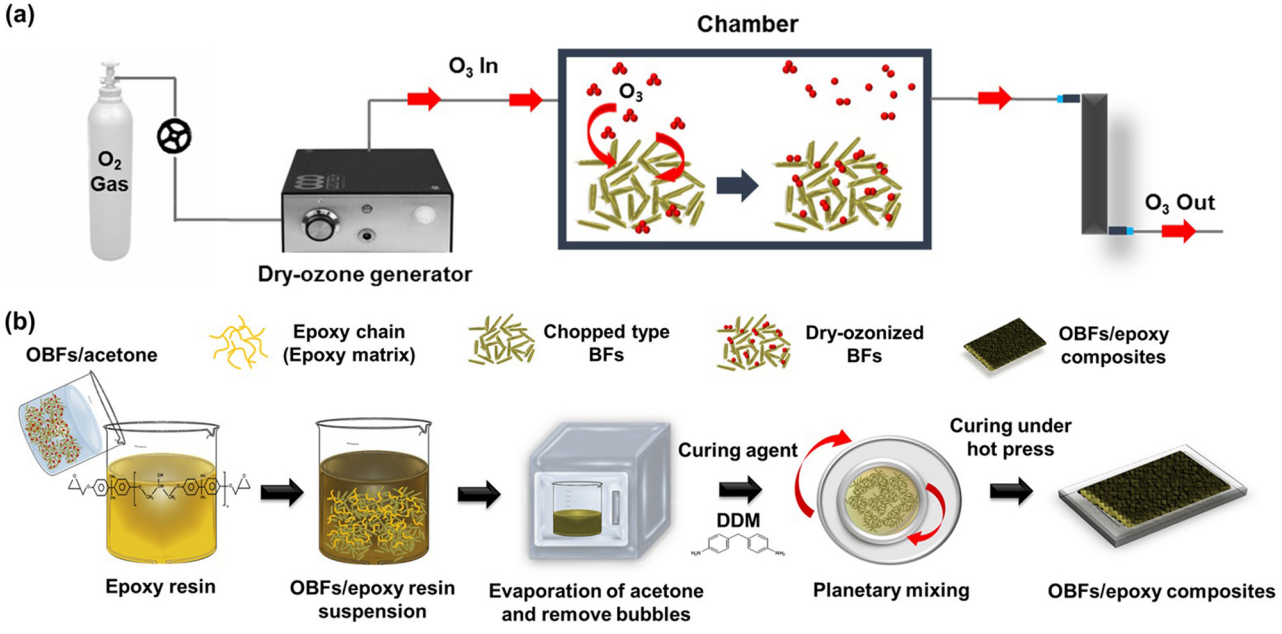

Figure 1: Schematic representation of OBFs/epoxy composites: (a) dry-ozone treatment of BFs and (b) composite preparation process.

OBFs (20, 40, 60, or 80 wt%) were added to an acetone/epoxy resin suspension and sonicated for 50 min at a power of 600 W (maximum temperature: 45°C). Thereafter, the mixture was heated in a vacuum oven at 100°C for 24 h to evaporate acetone. The curing agent (DDM) was added to the OBF/epoxy mixture and planetary mixed for approximately 5 min (planetary mixing is an efficient method to fabricate bubble-free composites). When the curing agent was dissolved, the resultant suspension was degassed at 70°C in the vacuum oven for 1 h to eliminate bubbles. After the bubble removal, the resulting mixture was continuously impregnated by BFs or OBFs using a three-roll milling machine for manufacturing the prepregs. Finally, the BF or OBF prepregs were cured at 80°C for 30 min, 110°C for 1 h, and 140°C for 2 h, and post-cured at 170°C for 2 h.

2.4 Characterization

X-ray diffraction (XRD, D2 Phaser, Bruker Co) was performed using the Cu-Kα radiation at 40 kV 40 mA^{-1} at scan steps of 0.02° from 10° to 80° to obtain XRD patterns of OBFs. Fourier-transform infrared vacuum spectroscopy (FT-IR, VERTEX 80 V, Bruker Co) was performed to evaluate the chemical states using KBr (radiation ranging from 500 to 4,000 cm^{-1}). X-ray photoelectron spectroscopy (XPS, K-alpha, Thermo Co) was performed to study the surface elements of OBFs using a monochromated Mg-Kα source (1486.6 eV). High-resolution scanning electron microscopy (HR-SEM, SU8010, Hitachi Co) was performed at an operating voltage of 20 kV to characterize the fracture surface of the composites after coating with platinum. Dynamic contact angles (DCAs) were tested using the sessile drop method on a dynamic contact angle meter (Phoenix 300 Plus/Touch, SEO Co). As proposed by Fowkes [27], Owens and Wendt [28], and Kaelble [29], the surface free energy can be calculated using equations (1) and (2):

$$\gamma = \gamma^{L} + \gamma^{SP}, \tag{1}$$

$$\gamma_L(1 + \cos\theta) = 2\left(\sqrt{\gamma_S^L \cdot \gamma_L^L} + \sqrt{\gamma_S^{sp} \cdot \gamma_L^{sp}}\right), \tag{2}$$

where γ is the total surface free energy, γ^L is the London dispersion component, γ^{SP} is the specific polar components, L represents a liquid, S represents a solid, and θ represents the DCAs [30]. The basic three-liquid data of surface free energy are provided in Table S1.

The universal testing machine (UTM, Lloyd LR5k, Lloyd-Instruments Co) was used to determine the fracture toughness (K_{IC}) of the composites in terms of the critical stress intensity factor, satisfying the requirements of ASTM E399. A span-to-depth ratio of 4:1 and a crosshead speed of 1 mm min^{-1} were considered. The fracture toughness of the specimens was calculated as follows [31,32]:

$$K_{IC} = \frac{FL}{bd^{3/2}} \cdot Y. \tag{3}$$

where F is the critical load; L is the span between the supports; b and d are the specimen thickness and characteristic length, respectively; and Y is the shape factor given by

$$Y = \frac{3a/d^{1/2}[1.99 - (a/d)(1 - a/d)(2.15 - 3.93a/d + (2.7a^2/d^2)]}{2(1 + 2a/d)(1 - a/d)^{3/2}}, \tag{4}$$

where a is the crack length. The precrack was cut to approximately half the specimen depth using a diamond razor blade (LSDC, DY Co).

The interlaminar shear strength (ILSS) of the specimens was evaluated using the UTM in three-point bending tests in accordance with ASTM D-2344 [33]. A span-to-depth ratio of 5:1 and a crosshead speed of 2 mm min^{-1} were considered. The ILSS determined from the specimens was calculated as (5)

$$\text{ILSS} = \frac{3F}{4bd}, \tag{5}$$

where the parameters are the same as those for K_{IC}.

3 Results and discussion

3.1 Characteristics of OBFs

XRD analysis was performed to investigate the crystallographic nature of BFs and OBFs, the results of which are shown in Figure 2(a). The XRD pattern indicates that a major portion of BFs has an amorphous structure [34,35]. The XRD pattern of the OBFs was similar to that of BFs, indicating that the amorphous structure and the interplanar spacing were the same. This indicates that the dry-ozonization process did not change the amorphous structure of BFs.

Figure 2(b) shows the FT-IR spectra of BFs before and after the dry-ozone treatment. After dry ozonization, the FT-IR spectra of OBFs exhibited a decrease in the peak at 914.6 cm^{-1} (corresponding to the Si–O–Si stretching vibrations) while new peaks appeared at 1636.7 and 3379.3 cm^{-1}, corresponding to the adsorbed water and Si–OH stretching vibrations, respectively refs. [36–38].

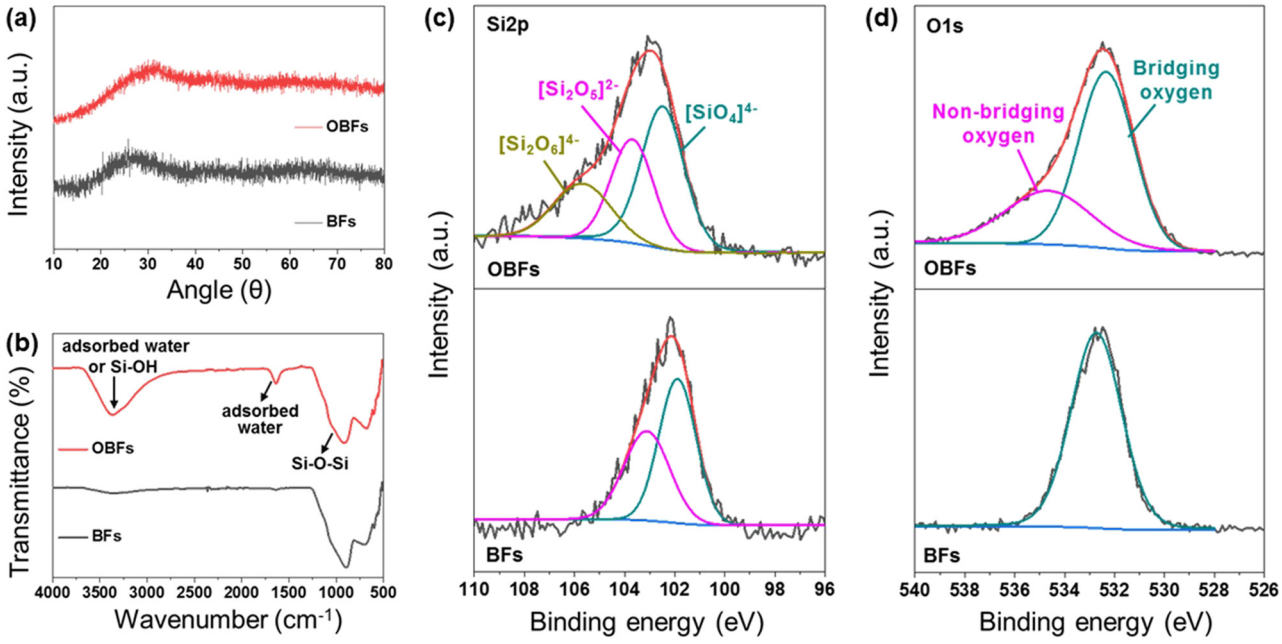

Figure 2: Characterization of BFs and OBFs: (a) XRD, (b) FT-IR spectra, (c) Si2p core level of XPS spectra, and (d) O1s core level of XPS spectra.

In dry-ozone treatment, the Si–O–Si network is attacked by OH^- and H^+. The reactions are explained by the following equations (6) and (7):

$$Si - O - Si + OH^- \rightarrow Si - OH + Si - O- \quad (6)$$

$$Si - O - SI + H^+ \rightarrow Si - OH + Si- \quad (7)$$

The OBF surfaces have a uniform structure because the OH^- and H^+ ions attack at ozonization.

In addition, for a detailed investigation on the surface elemental composition and chemical states of OBFs, the Si2p and O1s XPS spectra were deconvoluted, and the results are shown in Figure 2(c) and (d). There were mainly three silicate groups present in the Si2p core level spectrum (Figure 2(c)), and the corresponding binding energies were determined to be 102.5, 103.7, and 105.8 eV [19,38,39]. The peak at the binding energy, centered at 102.5 eV, can be attributed to $[SiO_4]^{4-}$ (tetrahedron structure). The peak at lower binding energy at 103.7 eV can be attributed to $[Si_2O_5]^{2-}$ of the layer shape structure. Similar to the FT-IR spectrum, a new peak corresponding to $[Si_2O_6]^{4-}$ (chain shape structure), derived from the oxygen end radicals, appeared at 105.8 eV [40,41]. To support this claim, direct evidence for the oxygen end radicals introduced on the surface of BFs can be obtained from the O1s peak deconvolution of OBFs shown in Figure 2(d). For the O1s core level spectra of BFs, only one peak was observed at 532.6 eV, corresponding to the bridging oxygen. However, the O1s core level spectra of OBFs divided into two peaks at 532.2 and 534.3 eV corresponded to the bridging oxygen and non-bridging oxygen, respectively. From the results for O1s spectra, the OBFs demonstrate the presence of non-bridging oxygen groups on the surface, which could enhance the interfacial adhesion between the fibers and the epoxy matrix. Thus, the FT-IR and XPS spectra demonstrate the presence of oxygen-containing functional groups on the surface of OBFs, which could affect the curing reaction of the epoxy resin.

3.2 Morphologies of OBFs

The microstructures of BFs and OBFs were observed by SEM, as shown in Figure 3(a and b). As evident in Figure 3(a), the BFs were fairly straight and highly ordered structures, and the outer surface was partially covered with a layer of metal oxide and starch. As shown in Figure 3(b), after dry ozonization, the surface of OBFs was very smooth with a few pits and grooves. This is because dry ozonization begins at the outer surface of BFs and progressively removes some of the metal oxide and starch by continuous O_3 oxidation. However, the fact that the highly ordered structure of OBFs is relatively clear proves that dry ozonization does not significantly disrupt the fiber structures.

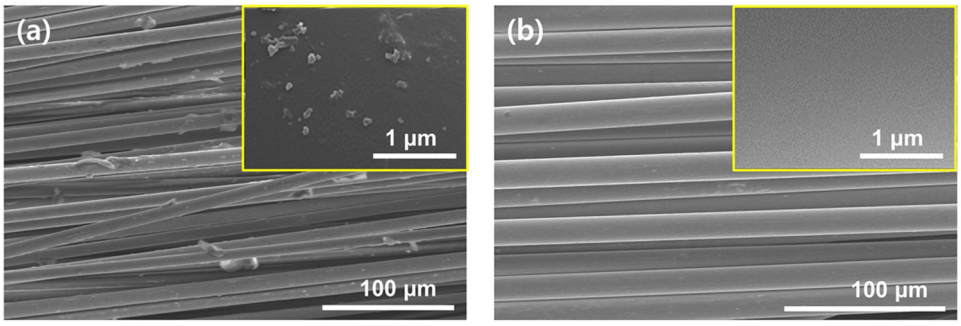

Figure 3: Surface morphology of BFs and OBFs: (a) SEM images of BFs and (b) OBFs.

3.3 Interfacial properties of OBF/epoxy composites

The surface free energy of the composites was closely related to the wettability between the fibers and epoxy matrix [42,43]. A high surface free energy can lead to better wettability and strong interfacial adhesion. The total surface free energy results for the OBF/epoxy composites are listed in Table S2 and shown in Figure 4(a). As expected, the BF/epoxy composites exhibited a low surface free energy due to the chemically inert BF surfaces. In contrast, the surface free energy of the OBF/epoxy composites was enhanced significantly compared to that of the BF/epoxy composites. Compared to the 20 wt% BF/epoxy composites (35.4 mJ m^{-2}), the surface free energy values for the 20 wt% OBF/epoxy composites (37.2 mJ m^{-2}) increased by 5.1%. Moreover, the measured highest surface free energy value was 39.7 mJ m^{-2} in the 60 wt% OBF/epoxy composites, leading to a 7.6% increase compared to that of the OBF/epoxy composites (36.9 mJ m^{-2}). In particular, the polar components of the OBF/epoxy composites exerted a greater influence on the surface free energy than the London dispersion components. The polar component of the BFs/epoxy composites reached roughly from ~6.4 to a maximum of ~7.8 mJ m^{-2}. In contrast, for the OBF/epoxy composites, the polar component increased significantly, ranging from ~7.5 to ~9.8 mJ m^{-2}, indicating that OBFs are more compatible with the polar epoxy matrixes. As demonstrated *via* FT-IR and XPS, the OBFs showed an increase in the oxygen-containing groups, which could be an important contributing factor for the improvement in the polar components [44,45].

To support this explanation, we performed a detailed study on the wetting behavior of distilled water (at 27°C for 5 min) acting on the composites. It can be seen from Figure 4(b) that the wetting behavior of the 60 wt% BF/epoxy composite indicates low wettability due to the chemically inactive surface of BFs, and the DCA is maintained at roughly 64.1°. In contrast, the wetting behavior of the 60 wt% OBF/epoxy composites decreased the DCAs rapidly and became saturated at approximately 41.8°.

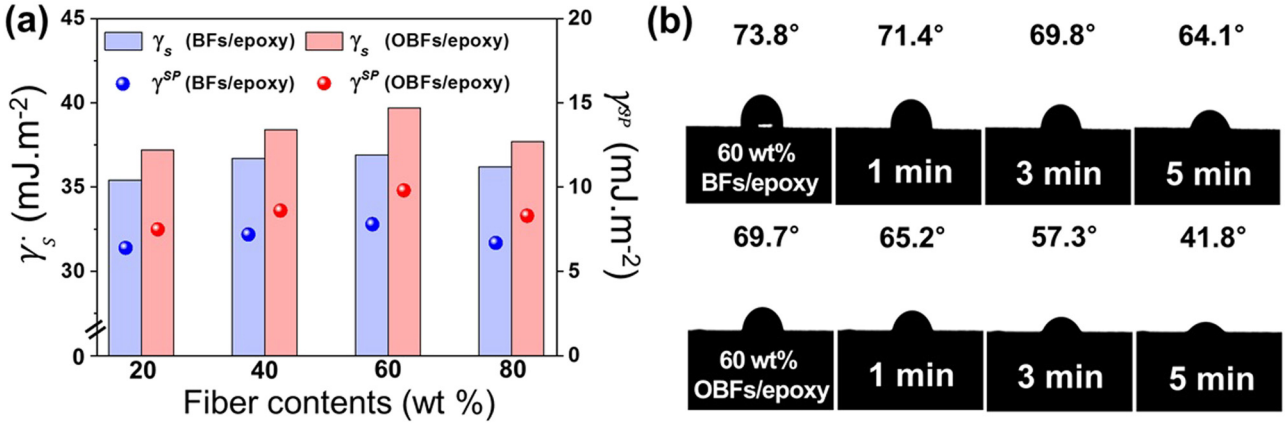

Figure 4: Interfacial interaction of BFs/epoxy and OBFs/epoxy composites: (a) surface free energy and (b) optical images of the DCA of distilled water over time.

This decrease is due to the oxygen-containing groups with a large number of hydrophilic surfaces on the OBFs from which water droplets could rapidly diffuse, thereby indicating enhanced wettability within the composites.

3.4 Mechanical properties of OBF/epoxy composites

The ILSS and K_{IC} can lay a solid foundation for the shear and fracture properties depending on the interfacial adhesion of the fibers within the epoxy matrix [46–48]. Therefore, the mechanical properties, including ILSS and K_{IC}, were studied for the OBF/epoxy composites to evaluate their efficiency. As shown in Figure 5, the OBF/epoxy composites revealed good linearity in the relationship between the mechanical properties and surface free energy. In addition, the OBF/epoxy composites showed significant improvements in the ILSS and K_{IC} values as compared to those of the BF/epoxy composites. Compared to the 20 wt% BF/epoxy composites, the ILSS and K_{IC} values of the 20 wt% OBF/epoxy composites increased by 43.0 and 22.5%, respectively. Moreover, the measured highest ILSS and K_{IC} values reached 33.8 MPa and 58.5 MPa $m^{1/2}$ in the 60 wt% OBF/epoxy composites, leading to a 21.2 and 23.2% increase compared to those in the 60 wt% BF/epoxy composites, respectively. These results indicate that the additional interfacial interlocking was active when OBFs were included within the epoxy matrix, and this enhanced the mechanical properties of the composites.

3.5 Interfacial mechanism of OBFs/epoxy composites

The schematic in Figure 6 depicts the interfacial mechanisms explaining the interfacial interlocking. As the crack opens, the cracks as shown in Figure 6(a) and (b) can occur, depending on the interfacial adhesion of the composites. For the BF/epoxy composites (Figure 6(a)), the crack paths can immediately extend to the fiber surface due to poor adhesion at the interface. Consequently, the composites could crack easily under a low load. In contrast, the OBF/epoxy composites (Figure 6(b)) prevented the cracks from contacting directly with the fiber surface, and crack paths could deviate into the interface area. This interface acted as a crack pinning that reduced the

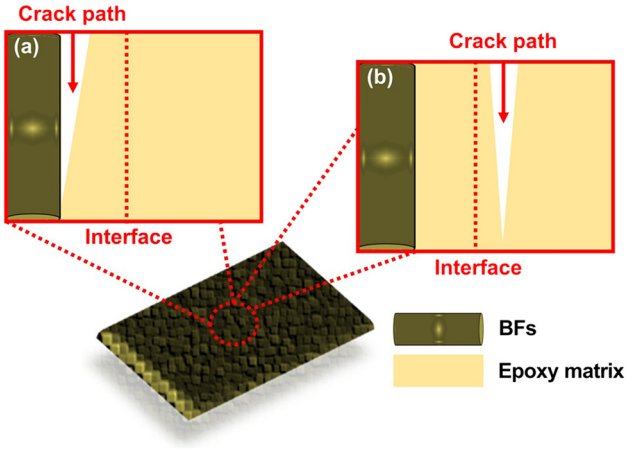

Figure 6: Schematic description of interfacial mechanism: (a) BFs/epoxy composite and, (b) OBFs/epoxy composites.

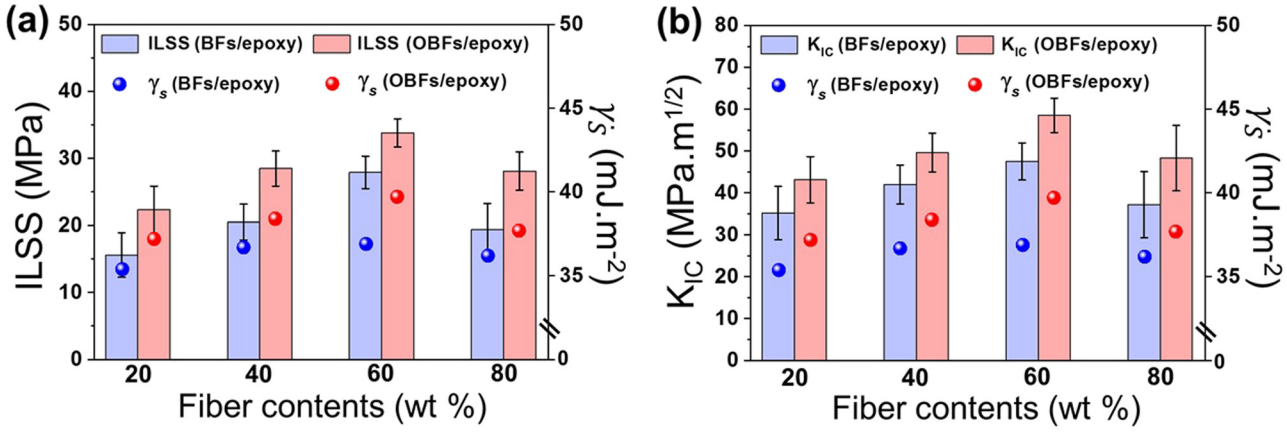

Figure 5: Mechanical properties of BFs/epoxy and OBFs/epoxy composites: (a) ILSS and (b) fracture toughness.

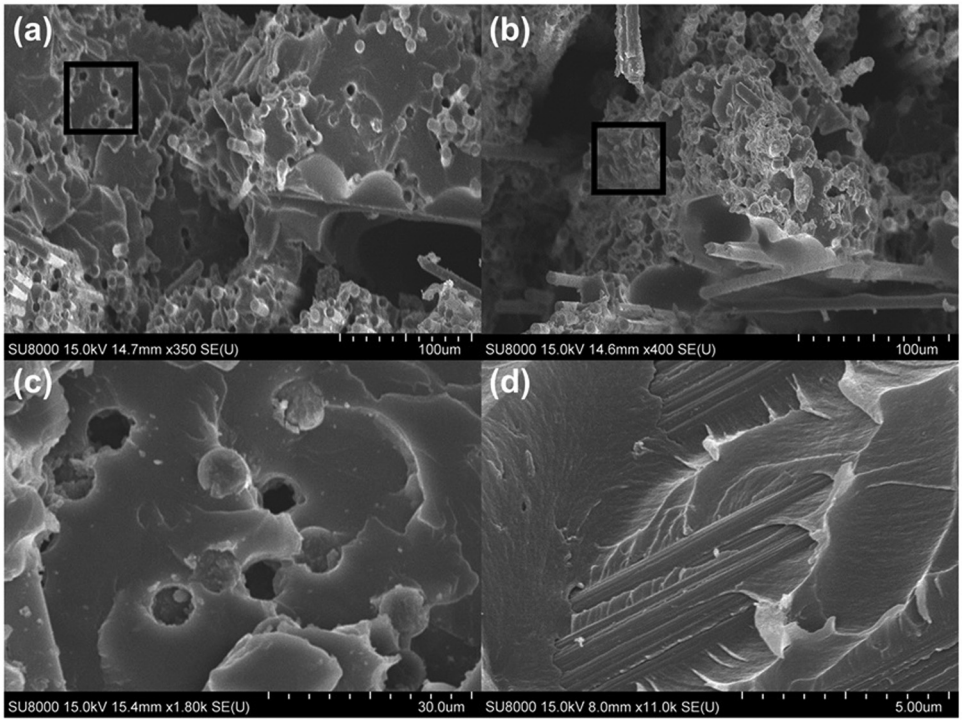

Figure 7: Fracture surfaces of BFs/epoxy and OBFs/epoxy composites: (a) 60 wt% BFs/epoxy composites, (b) 60 wt% OBFs/epoxy composites, (c) and (d) the magnified fractured surface of the closed regions in (a) and (b), respectively.

internal stress concentration and enhanced the energy dissipation during deformation.

Some evidence for these interfacial mechanisms could be demonstrated on the presented fractured surfaces. Figure 7(a–d) displays SEM images of the fractured surfaces of the BF/epoxy and OBFs/epoxy composites. For the 60 wt% BF/epoxy composites (Figure 7(a) and (c)), there are distinct cracks between the BFs and the epoxy matrix. Consequently, the interfacial debonding occurred on the BF surfaces; the BFs were totally detached from the resin, and a large number of holes remained in the epoxy matrix. In contrast, the 60 wt% OBF/epoxy composites exhibited crack progression almost proprietarily along the rich interfaces and were tightly embedded within an epoxy matrix without de-bonding (Figure 7(b) and (d)). This inhibits propagation through the epoxy matrix as a crack must pass either through or fiber regions with epoxy-rich interfaces, resulting in enhanced mechanical properties.

4 Conclusion

In summary, OBFs were effectively utilized as reinforcements to enhance the interfacial adhesion of composites. The results show that OBFs can enhance the interfacial adhesion of composites, thereby leading to a significant enhancement in both ILSS and K_{IC}. The enhanced interfacial adhesion was attributed to the oxygen end radicals introduced to the OBF surfaces, which can penetrate deep and stably into the epoxy matrix. In this regard, the measured highest ILSS and K_{IC} values reached 33.8 MPa and 58.5 MPa $m^{1/2}$ with 60 wt% OBF/epoxy composites, indicating 21.2 and 23.2% enhancement compared to the 60 wt% BF/epoxy composites. Our results demonstrate that the hierarchical OBF/epoxy composites with outstanding interfacial adhesions and mechanical properties obtained through simple and commercial manufacturing are attractive candidates for fabricating new types of structural-functional integrated composites.

Funding information: This work was supported by the "Policy R&D program KPP20002-2" funded by the Korea Institute of Ceramic Engineering and Technology, Republic of Korea, and the Technological Innovation R&D Program (S2829590) funded by the Small and Medium Business Administration (SMBA, Korea).

Author contributions: All authors have accepted responsibility for the entire content of this manuscript and approved its submission.

Conflict of interest: The authors state no conflict of interest.

Data availability statement: The datasets generated during and/or analysed during the current study are available in the Supplementary material on the journal website.

References

[1] Robertson ID, Yourdkhani M, Centellas PJ, Aw JE, Ivanoff DG, Goli E, et al. Rapid energy-efficient manufacturing of polymers and composites via frontal polymerization. Nature. 2018;557(7704):223–7.

[2] Yang K, Guan J, Numata K, Wu C, Wu S, Shao Z, et al. Integrating tough Antheraea pernyi silk and strong carbon fibres for impact-critical structural composites. Nat Commum. 2019;10(1):1–12.

[3] Taynton P, Ni H, Zhu C, Yu K, Loob S, Jin Y, et al. Repairable woven carbon fiber composites with full recyclability enabled by malleable polyimine networks. Adv Mater. 2016;28(15):2904–9.

[4] Yao Z, Wang C, Qin J, Su S, Wang Y, Wang Q, et al. Interfacial improvement of carbon fiber/epoxy composites using one-step method for grafting carbon nanotubes on the fibers at ultra-low temperatures. Carbon. 2020;164:133–42.

[5] Wu Q, Zhao R, Xi T, Yang X, Zhu J. Comparative study on effects of epoxy sizing involving ZrO_2 and GO on interfacial shear strength of carbon fiber/epoxy composites through one and two steps dipping routes. Compos Pt A-Appl Sci Manuf. 2020;134:105909.

[6] Han J, Wang D, Zhang P. Effect of nano and micro conductive materials on conductive properties of carbon fiber reinforced concrete. Nanotechnol Rev. 2020;9(1):445–54.

[7] Tapper RJ, Longana ML, Norton A, Potter KD, Hamerton I. An evaluation of life cycle assessment and its application to the closed-loop recycling of carbon fibre reinforced polymers. Compos Pt B-Eng. 2020;184:107665.

[8] Zakaria MR, Akil HM, Omar MF. Abdullah MMAB, Ab Rahman AA, Othman MBH. Improving flexural and dielectric properties of carbon fiber epoxy composite laminates reinforced with carbon nanotubes interlayer using electrospray deposition. Nanotechnol Rev. 2020;9(1):1170–82.

[9] Dhand V, Mittal G, Rhee KY, Park SJ, Hui D. A short review on basalt fiber reinforced polymer composites. Compos Pt B-Eng. 2015;73:166–80.

[10] Kim SH, Park SJ, Rhee KY, Park SJ. Effects of ozonized carbon black on fracture and post-cracking toughness of carbon fiber-reinforced epoxy composites. Compos Pt B-Eng. 2019;177:107379.

[11] Zhang Y, Yu C, Chu PK, Lv F, Zhang C, Ji J, et al. Mechanical and thermal properties of basalt fiber reinforced poly (butylene succinate) composites. Mater Chem Phys. 2012;133(2–3):845–9.

[12] Ying Z, Wu D, Zhang M, Qiu Y. Polylactide/basalt fiber composites with tailorable mechanical properties: effect of surface treatment of fibers and annealing. Compos Struct. 2017;176:1020–7.

[13] Zhou S, Wang J, Wang S, Ma X, Huang J, Zhao G, et al. Facile preparation of multiscale graphene-basalt fiber reinforcements and their enhanced mechanical and tribological properties for polyamide 6 composites. Mater Chem Phys. 2018;217:315–22.

[14] Seghini MC, Touchard F, Sarasini F, Cech V, Chocinski-Arnault L, Mellier D, et al. Engineering the interfacial adhesion in basalt/epoxy composites by plasma polymerization. Compos Pt A-Appl Sci Manuf. 2019;122:67–76.

[15] Zhu H, Wu G, Zhang L, Zhang J, Hui D. Experimental study on the fire resistance of RC beams strengthened with near-surface-mounted high-Tg BFRP bars. Compos Pt B-Eng. 2014;60:680–7.

[16] Xie J, Yao L, Xu F, Li Y, Shan Z, Hui D, et al. Fabrication and characterization of three-dimensional PMR polyimide composites reinforced with woven basalt fabric. Compos Pt B-Eng. 2014;66:268–75.

[17] Balaji KV, Shirvanimoghaddam K, Rajan GS, Ellis AV, Naebe M. Surface treatment of Basalt fiber for use in automotive composites. Mater Today Chem. 2020;17:100334.

[18] Lee SO, Rhee KY, Park SJ. Influence of chemical surface treatment of basalt fibers on interlaminar shear strength and fracture toughness of epoxy-based composites. J Ind Eng Chem. 2015;32:153–6.

[19] Kim MT, Kim MH, Rhee KY, Park SJ. Study on an oxygen plasma treatment of a basalt fiber and its effect on the interlaminar fracture property of basalt/epoxy woven composites. Compos Pt B-Eng. 2011;42(3):499–504.

[20] Kim SH, Heo YJ, Park SJ. Ozonization of SWCNTs on thermal/mechanical properties of basalt fiber-reinforced composites. Steel Compos Struct. 2019;31(5):517–27.

[21] Sun X, Liu X, Shen X, Wu Y, Wang Z, Kim JK. Reprint of Graphene foam/carbon nanotube/poly (dimethyl siloxane) composites for exceptional microwave shielding. Compos Pt A-Appl Sci Manuf. 2017;92:190–7.

[22] Luo J, Liu Y, Wei H, Wang B, Wu KH, Zhang B, et al. A green and economical vapor-assisted ozone treatment process for surface functionalization of carbon nanotubes. Green Chem. 2017;19(4):1052–62.

[23] Gong J, Liu Y, Sun X. O_3 and UV/O_3 oxidation of organic constituents of biotreated municipal wastewater. Water Res. 2008;42(4–5):1238–44.

[24] Alaton IA, Balcioglu IA, Bahnemann DW. Advanced oxidation of a reactive dyebath effluent: comparison of O_3, H_2O_2/UV-C and TiO_2/UV-A processes. Water Res. 2002;36(5):1143–54.

[25] Wang Q, Shi W, Zhu B, Su DS. An effective and green H_2O_2/H_2O/O_3 oxidation method for carbon nanotube to reinforce epoxy resin. J Mater Sci Technol. 2020;40:24–30.

[26] Downey MA, Drzal LT. Toughening of carbon fiber-reinforced epoxy polymer composites utilizing fiber surface treatment and sizing. Compos Pt A-Appl Sci Manuf. 2016;90:687–98.

[27] Fowkes FM. Determination of interfacial tensions, contact angles, and dispersion forces in surfaces by assuming additivity of intermolecular interactions in surfaces. J Phys Chem. 1962;66(2):382–2.

[28] Owens DK, Wendt RC. Estimation of the surface free energy of polymers. J Appl Polym Sci. 1969;13(8):1741–7.

[29] Kaelble DH. Dispersion-polar surface tension properties of organic solids. J Adhes. 1970;2:66–81.

[30] Park SJ, Brendle M. London dispersive component of the surface free energy and surface enthalpy. J Colloid Interface Sci. 1997;188(2):336–9.
[31] Cha J, Jun GH, Park JK, Kim JC, Ryu HJ, Hong SH. Improvement of modulus, strength and fracture toughness of CNT/Epoxy nanocomposites through the functionalization of carbon nanotubes. Compos Pt B-Eng. 2017;129:169–79.
[32] Kim SH, Rhee KY, Park SJ. Amine-terminated chain-grafted nanodiamond/epoxy nanocomposites as interfacial materials: thermal conductivity and fracture resistance. Compos Pt B-Eng. 2020;192:107983.
[33] Bisht A, Dasgupta K, Lahiri D. Investigating the role of 3D network of carbon nanofillers in improving the mechanical properties of carbon fiber epoxy laminated composite. Compos Pt A-Appl Sci Manuf. 2019;126:105601.
[34] Kwak BS, Kim KM, Park SM, Kang M. Synthesis of basalt fiber@ Zn1-xMgxO core/shell nanostructures for selective photoreduction of CO_2 to CO. Appl Surf Sci. 2017;407:109–16.
[35] Zhao X, Ouyang J, Yang H, Tan Q. Effect of Basalt fibers for reinforcing resin-based brake composites. Minerals. 2020;10(6):490.
[36] Arslan C, Dogan M. The effects of silane coupling agents on the mechanical properties of basalt fiber reinforced poly butylene terephthalate) composites. Compos Pt B-Eng. 2018;146:145–54.
[37] Wei B, Song S, Cao H. Strengthening of basalt fibers with nano-SiO_2-epoxy composite coating. Mater Des. 2011;32(8–9):4180–6.
[38] Paukshtis EA, Yaranova MA, Batueva IS, Bal'zhinimaev BSA. FTIR study of silanol nests over mesoporous silicate materials. Microporous Mesoporous Mat. 2019;288:109582.
[39] Zhang X, Zhou X, Ni H, Rong X, Zhang Q, Xiao X, et al. Surface modification of basalt fiber with organic/inorganic composites for biofilm carrier used in wastewater treatment. ACS Sustain Chem Eng. 2018;6(2):2596–602.
[40] Wang ZT, Luo HJ, Zhang L, Zhang J, Chen HW, Jiang H. Mechanical properties of basalt fiber improved by starch phosphates sizing agent. Applied Surface Science. 2020;521:146196.
[41] Wang J, Zhou S, Huang J, Zhao G, Liu Y. Interfacial modification of basalt fiber filling composites with graphene oxide and polydopamine for enhanced mechanical and tribological properties. RSC Adv. 2018;8(22):12222–31.
[42] Jiang Q, Tallury SS, Qiu Y, Pasquinelli MA. Interfacial characteristics of a carbon nanotube-polyimide nanocomposite by molecular dynamics simulation. Nanotechnol Rev. 2020;9(1):136–45.
[43] Park JM, Kim DS, Kim SR. Improvement of interfacial adhesion and nondestructive damage evaluation for plasma-treated PBO and Kevlar fibers/epoxy composites using micromechanical techniques and surface wettability. J Colloid Interface Sci. 2003;264(2):431–45.
[44] Liu Y, Jiang X, Shi J, Luo Y, Tang Y, Wu Q, et al. Research on the interface properties and strengthening–toughening mechanism of nanocarbon-toughened ceramic matrix composites. Nanotechnol Rev. 2020;9(1):190–208.
[45] Zakaria MR, Akil HM, Omar MF, Abdullah MMAB, Ab Rahman AA, Othman MBH. Improving flexural and dielectric properties of carbon fiber epoxy composite laminates reinforced with carbon nanotubes interlayer using electrospray deposition. Nanotechnol Rev. 2020;9(1):1170–82.
[46] Khandelwal S, Rhee KY. Recent advances in basalt-fiber-reinforced composites: tailoring the fiber-matrix interface. Compos Pt B-Eng. 2020;192:108011.
[47] Golewski GL. Estimation of the optimum content of fly ash in concrete composite based on the analysis of fracture toughness tests using various measuring systems. Constr Build Mater. 2019;213:142–55.
[48] Adak NC, Chhetri S, Kuila T, Murmu NC, Samanta P, Lee JH. Effects of hydrazine reduced graphene oxide on the interlaminar fracture toughness of woven carbon fiber/epoxy composite. Compos Pt B-Eng. 2018;149:22–30.